CFD Letters

Journal homepage:
https://semarakilmu.com.my/journals/index.php/CFD_Letters/index
ISSN: 2180-1363

Parametric Optimization for Power Generation of Flow Induced Vibration Energy Harvester

Muhammad Hanif Razali[1], Khairul Affendy Md Nor[1,*], Mohd Azan Mohammed Sapardi[1], Nor Hidayati Diyana Nordin[1], Fadhlan Hafizhelmi Kamaru Zaman[2], Azlee Zabidi[3]

[1] Kulliyyah of Engineering, International Islamic University Malaysia, Gombak, 53100 Kuala Lumpur, Malaysia
[2] College of Engineering, Universiti Teknologi MARA, 40450 Shah Alam, Selangor, Malaysia
[3] Faculty of Computing, Universiti Malaysia Pahang Al-Sultan Abdullah, 26600 Pekan, Pahang, Malaysia

ARTICLE INFO

Article history:
Received 20 March 2024
Received in revised form 21 April 2024
Accepted 19 May 2024
Available online 31 October 2024

Keywords:
flow-induced vibration (FIV); vortex-induced vibration (VIV); wake-induced vibration (WIV); Reynolds number; piezoelectric; gap length

ABSTRACT

Flow-induced vibration occurs when the motion of fluids through a structure induces oscillations or vibrations in the structure. An effective flow-induced vibration energy harvester has substantial challenges due to the river's irregular velocity flows. It is not practicable to use one parameter for all velocities. This work presents the testing of a flow-induced vibrational energy harvester in laminar flow using two circular cylinders positioned in tandem within an open-channel flow. A CFD simulation using COMSOL Multiphysics was performed for the proposed parameter. A comprehensive simulation run at multiple Reynolds numbers with varying gap lengths between the bluff bodies is studied to determine the maximum power generated. Simulation results show that the optimal gap lengths for Re 60, 80, 100, 120, 140, and 160 are 8.5, 6.0, 3.0, 3.0, 3.5, and 4.5, respectively. These gap lengths result in power outputs of 0.0315 W, 2.616 W, 1.899 W, 0.6552 W, 0.5018 W, and 0.3782 W. By demonstrating the relationship between Reynolds number and gap length, this study provides important information for maximising the energy harvesting from flow-induced vibration (FIV).

1. Introduction

In response to increasing energy consumption and environmental concerns, there has been a growing interest in renewable energy sources. Fossil fuel dependence and its contribution to global warming have highlighted the need for sustainable alternatives. Fluid dynamics has become a developing area of study for researchers in energy harvesting. Computational Fluid Dynamics (CFD) is crucial in performing simulations and obtaining numerical solutions for the complex problems associated with fluid mechanics models. For instance, Arif *et al.,* [1] employed Computational Fluid Dynamics (CFD) to address issues pertaining to fluid flow and heat transmission. With the advancement in computational power, integrating physics-informed deep learning methodologies stands to enhance and refine the numerical simulation process, as supported by recent research findings [2, 3]. Approaches based on deep learning can achieve a balance between the effectiveness

* *Corresponding author.*
E-mail address: affendy@iium.edu.my (Khairul Affendy Md Nor)

https://doi.org/10.37934/cfdl.17.3.109123

and precision of data prediction. Furthermore, deep learning methodologies can significantly improve computational efficiency and reliability analysis.

Flow-induced vibration (FIV) phenomena have emerged as a promising avenue for converting fluid flow energy into electrical energy. This approach harnesses the natural motion of flowing fluids, offering a sustainable solution to meet rising energy demands. The utilization of renewable energy aligns with the Sustainable Development Goals (SDG7) and provides affordable, reliable, and sustainable energy access. Adopting and implementing these technologies can effectively reduce the adverse effects of climate change while fostering the development of a resilient energy infrastructure.

The discovery has enormous implications for advancing flow-induced vibration energy harvesting technologies, particularly for sustainable power generation for devices with low energy consumption. This advancement is essential because of the increasing need for low-power devices such as micro-electromechanical systems (MEMS) and wireless sensor networks. This application extensively affects multiple industries, from environmental monitoring to healthcare, guaranteeing continuous device operation while minimizing environmental consequences.

FIV encompasses various oscillations arising from the interaction between fluids and structures. Vortex-induced vibration (VIV) and wake-induced vibration (WIV) are two notable categories within FIV. Pinar *et al.,* [4], Zahari and Dol [5], Atrah *et al.,* [6] and Naseer *et al.,* [7] have extensively studied VIV, focusing on the pressure dynamics surrounding a vibrating cylinder in the presence of fluid viscosity. The flow passing the cylinder generates separated shear layers on its top and bottom sides, impeding kinetic energy transfer downstream. Consequently, pressure differences fluctuate between the upper and lower sides of the cylinder, inducing vibrations. Zhang & Wang [8] discovered that resonance occurs when vortex shedding frequency matches the cylinder's natural frequency, resulting in synchronized vibrations. The mass-damping ratio influences the amplitude.

WIV occurs when a group of bluff bodies are arranged in an array and exposed to a flowing stream. As the stream flow interacts with the upstream cylinder, it creates a wake, resulting in low-pressure regions and generating pressure differences around the downstream cylinder. These pressure differences induce vibrations in the downstream cylinder. Similar to VIV, WIV involves pressure differences around a cylinder. However, the crucial distinction lies in the influence of wakes formed by other cylinders on these pressure differences. Zhang & Wang [8] demonstrated that WIV exhibits a higher energy production capacity compared to VIV, reinforcing this finding.

An additional influential factor impacting the cylinder's amplitude pertains to the bluff body's geometric attributes. Variations in geometry give rise to distinct patterns of vortex shedding. Han *et al.,* [9] conducted an empirical study to evaluate the effectiveness of a square cylinder with three distinct incident angles. Overall, all three incident angles produced low energy harvesting efficiency, primarily due to the square cylinder's geometric configuration, which naturally produces low vibration frequencies and reduced amplitudes. In a related study, Abdelkefi *et al.,* [10] suggested an experiment to check how well an energy-gathering system works when it uses cylinders with different cross-sectional shapes. Their research showed that isosceles triangles with a base angle of 30° and square shapes were better at voltage at lower flow rates than isosceles triangles with a base angle of 90° and other isosceles shapes. Researchers tested an experiment with various setups in wind tunnels and cross-sectional geometries, including square, circle, semi-circle, and triangle [11]. The results showed that in a single-cylinder arrangement, the amplitude of triangular and square cylinders is greater than that of semi-circular and circular cylinders. However, when arranged in tandem, the circular cylinders exhibited the highest recorded amplitude.

The cylinder arrangement, such as tandem, cross-flow, and inline, also plays a significant role in this area. Ássi [12] and Ássi *et al.,* [13] discovered that tandem arrangements produce amplitudes

50% higher than those in isolated cylinder experiments. Figure 2.6 showed the arrangement of the cylinders in tandem. According to Fan *et al.,* [14], the vibration of the cylinder in tandem arrangement increases due to the high wake disturbance. Meanwhile, in inline and cross-flow arrangements, the vibration of the cylinders is lower than in tandem. Therefore, we implemented the same arrangement in tandem using a circular cylinder in this experiment.

Dahl *et al.,* [15] and Wang *et al.,* [16] stated that the Reynolds number effect significantly affects the amplitude response of the cylinder in FIV. Raghavan *et al.,* [17] supported the statement by proving that Re significantly affects amplitude ratio compared to mass ratio. Govardhan *et al.,* [18] achieved an understanding of the Re in FIV phenomenon through an experiment. The cylinder's amplitude response increases as Re increases.

According to Ássi *et al.,* [13] in the same size upstream and downstream cylinder experiment, there is the best distance between both cylinders that will increase the amplitude vibration of the downstream cylinder. Therefore, we can produce a higher-efficiency energy harvester. Hassim *et al.,* [19] discovered the vital parameter in FIV energy harvesting, the gap ratio, which has a significant impact on WIV. The experiment found that the cylinder's vibration increased between gap lengths 2D and 3D, where the optimal gap is 2.5D, which produces the highest lift coefficient due to the instability of the flow. Zhang & Wang [8] stated that the synchronous phenomenon takes place at the critical gap length. The synchronous phenomenon occurs when the vortex shedding frequency matches the cylinder's natural frequency. The synchronous phenomenon is important in FIV because it results in maximum vibration amplitude.

Harvesting energy from water flow with FIV energy harvesters yields higher outputs than wind flow, primarily due to the higher density of water in comparison to air. The substantial difference in density results in a significantly greater amount of energy stored within the water flow, enhancing the potential for energy extraction. The current challenge impeding the widespread adoption of flow-induced vibration energy harvesters in the river is the inconsistent velocity of the river flows. These variations pose significant obstacles to achieving optimal efficiency in energy harvesting processes. River velocities influence the power generated by the energy harvester. Therefore, the use of a single parameter for different velocities could be more practical. Hence, this research aims to identify and analyze the relation between the gap length and the Reynolds number to obtain the optimum power output for different velocities of the water flow. Throughout the test, the downstream and upstream cylinder diameters remained constant.

This paper consists of five distinct sections. Section 2 explores the simulation study, detailing the methodology and approach employed. Following this, Section 3 presents the data collection approach, while Section 4 discusses the simulation data and engages in a comprehensive discussion. Lastly, Section 5 provides concluding remarks, summarizing the key findings and offering insights for future research directions.

2. Simulation Study

In this research, numerical simulations using COMSOL Multiphysics were conducted to investigate power generation from piezoelectric sources systematically. The simulation model of the FIV energy harvester was placed in an open-channel flow to replicate the river. Laminar flow was studied in this simulation. The simulation for laminar flow aims to determine optimal parameters for power generation, given that the optimal performance of FIV energy harvesters was set in laminar conditions. The laminar flows were studied with a specific focus on two key parameters: the Reynolds number and the gap length between the upstream and downstream cylinders, which influence the formation of Karman vortices behind the cylinder. In this simulation, six different sets of Reynolds

numbers have been tested, starting from Re 60 to Re 160, with 20 steps. The gap length in each set is varied using a parametric sweep function from n = 2 to n = 9.5 with a 0.5 increment in each set.

2.1 Reynolds Number

The first parameter can be modified by adjusting the Reynolds number by varying the speed of the water flow in accordance with the Reynolds number formula, as shown below:

$$\mathrm{Re} = \frac{\rho UD}{\mu} \tag{1}$$

Where ρ is a constant parameter for water density, U is the speed of the water flow, D is the characteristic dimension and is the fluid dynamic viscosity. The speed of water tested was from 0.75 m/s for Re 60 to 2.0 m/s for Re 160, with a 0.25 m/s increment for every set. An increase in the speed of the water flow will increase the Reynolds number. The value of speed is decided based on the speed of the river obtained in an experiment conducted by Shafiai *et al.,* [19]. The value of U is multiplied by an equation to emulate a steady flow, providing precision and applicability in the simulation setup. The expression used is shown below:

$$U*2[m/s]*Y*(0.41[m]-Y)*step1(t/1[s])/(0.5*0.41[m]\text{^}2 \tag{2}$$

where U is the speed of the water flow and Y represents a spatial variable, denoting a distance along the axis.

2.2 Gap Length between Cylinders

The gap length between cylinders is the other parameter, as varying the gap length will have a significant impact on the amplitude of the induced vibration at the downstream cylinder. The upstream and downstream cylinders are arranged in a tandem arrangement. The size of the gap length between both cylinders, n, will be the factor of the cylinder diameter, D, where n is a dimensionless unit. Downstream and upstream cylinders will have the same diameter in this simulation. The upstream cylinder was set to be rigid during the simulation and will be moved further from the downstream cylinder in each set of data to increase the gap length, n. The parametric sweep feature automates the process of systematically modifying the value of gap length after the completion of each set, as illustrated in Figure 1. Once all sets within the first Reynolds number range are completed, the second Re will be manually adjusted, initiating a continuation through the subsequent sets until the final Reynolds number range is covered.

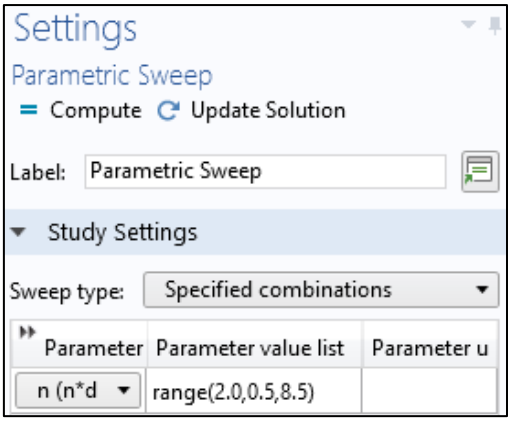

Fig. 1. Parametric sweep feature

2.3 Simulation Setup

The downstream cylinder was independently mounted on an elastic beam to oscillate transversely in the flow direction. The parameter and domain settings are shown in Figure 2. The inlet velocity and outlet pressure were both fixed at the inlet and outlet boundaries, respectively, and the wall condition was established as a no-slip wall. Both walls were set to open boundaries to replicate the open-channel flow. The parameter Vin is the normal inflow velocity, and LCH is the length of the testing channel with the flow size L × 0.35L. The fluid used in the simulation was water.

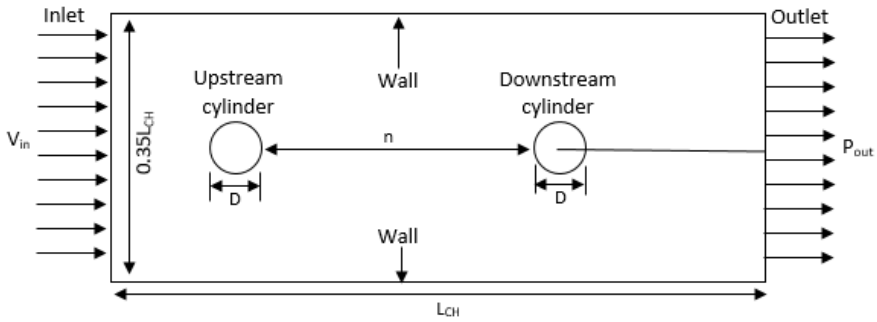

Fig. 2. Parameters and domain setting of the simulation

Figure 3 shows the 3D schematic diagram of the FIV energy harvester. A piezoelectric sheet attached to the fixed end of a cantilever beam harnesses flow-induced vibration. The cantilever beam remains fixed at one end and is connected to the bluff body known as the downstream cylinder at the other end. When the water flows past the upstream cylinder, it generates vortices behind it. The alternating vortices produced induce oscillations in the downstream cylinder, consequently leading to oscillations in the cantilever beam. The piezoelectric sheet exhibits the piezoelectric effect by converting mechanical energy into electrical energy through the oscillations of the cantilever beam.

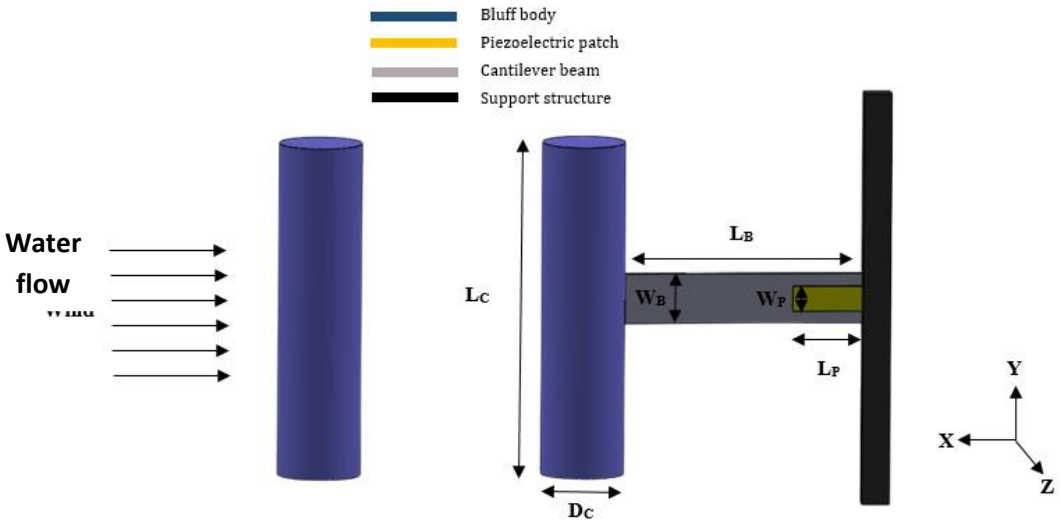

Fig. 3. 3D schematic diagram of FIV energy harvester

As illustrated in Figure 3, L_C and D_C are the length and diameter of bluff body respectively. Both bluff bodies have the same dimension. L_B and W_B are the length and width of cantilever beam while L_P and W_P are the length and width of piezoelectric. Table 1 displayed the parameter of the FIV energy harvester.

Table 1
Parameters of the FIV energy harvester

Component	Parameters	Values	Units
Cylinder diameter	D_C	40	mm
Cylinder length	L_C	200	mm
Beam length	L_B	220	mm
Beam width	W_B	26	mm
Beam thickness	T_B	2	mm
PZT length	L_P	40	mm
PZT width	W_P	10	mm
PZT Thickness	T_p	0.8	mm

In this simulation study, the model is meshed into 13834 triangular prism elements. The mesh was divided into two categories: fluid dynamics and general physics, as shown in Figure 4. Fluid dynamics calibration consists of two domains, blue and grey. General physics calibration consists of one domain, which is the yellow domain.

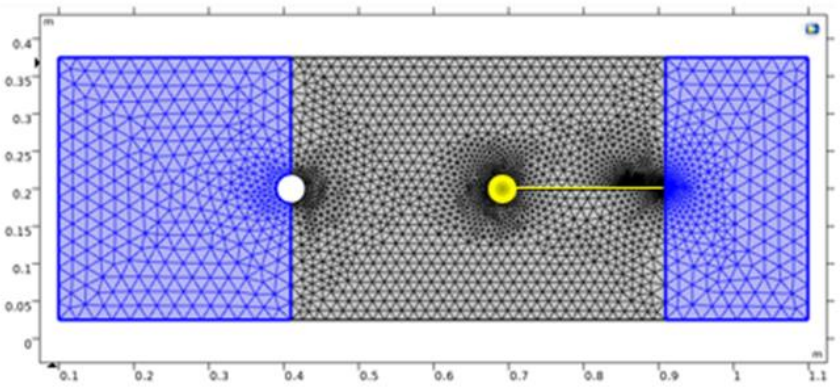

Fig. 4. Mesh of CFD model

Material properties were defined in every geometric entity of the model to optimize the modeling processes. The upstream and downstream cylinders are set to polyvinyl chloride (PVC). The elastic beam, piezoelectric, and fluid used in this simulation are set to aluminum, lead zirconate titanate (PZT-5H), and water (H2O), respectively.

Multiphysics interfaces in COMSOL Multiphysics are used to simplify the complex mathematical modeling required for simulations. In this simulation, two types of Multiphysics are utilised: fluid-structure interaction and the piezoelectric effect. Fluid-structure interaction consists of solid mechanics physics and laminar flow. The interrelation between these two physics is important in interacting with the flow of water with the structure beam. The default setup is used in the Solid Mechanics physics setting. The Laminar Flow Physics interface is configured to simulate the dynamic nature of laminar fluid flow phenomena.

Piezoelectric Effect Multiphysics consists of solid mechanics and electrostatics. This coupling comprehensively represents the full extent of the piezoelectric effect, where mechanical deformations on the piezoelectric strip induce electric fields when the beam oscillates during simulation. The default setting is used in both physics**.**

A workstation PC was used to simulate the experiment. However, there are limitations due to the PC's hardware constraints, like the processor and memory capacity, which affected the quality and extent of simulations in Comsol Multiphysics. Higher Reynolds numbers demanded more computing power, resulting in longer simulation times and narrowing the range of feasible parameters. These constraints may have influenced the findings, though efforts were made to optimize settings.

3. Data Collection Approach

This part describes the steps that were taken to collect the data. These include looking at velocity flow patterns, getting lift force, cylinder displacement, and voltage generated, and finally figuring out the power generated for each simulated Reynolds number within certain gap lengths.

Figure 5 presents the velocity flow patterns at Reynolds number 80, offering a visual representation of the fluid velocity distribution as it circulates the cylinder. Using streamlines, the table displays variations in velocity at different locations within the flow field. Regions highlighted in red denote high-velocity flow, while those in blue indicate low-velocity flow.

The initial figure in Figure 5(a) illustrates the laminar flow entering from the inlet. At t = 0.90s, the flow makes contact with the upstream cylinder, causing the wake to form. By t = 2.1s, the early stages of wake interference become apparent. As time progresses to t = 4.55s, the downstream cylinder begins to oscillate, primarily influenced by the wake's interference. Figure 5(e) and Figure 5(f) demonstrate the ongoing oscillation of the downstream cylinder. The distinct velocity flows generated in the wake region result in different pressure areas. The wake area typically experiences low pressure compared to the surrounding flow. For example, when t = 8.15s, the high-pressure region at the top of the downstream cylinder pushes it downward. In contrast, at t = 9.0s, the high pressure at the bottom of the cylinder results in upward movement.

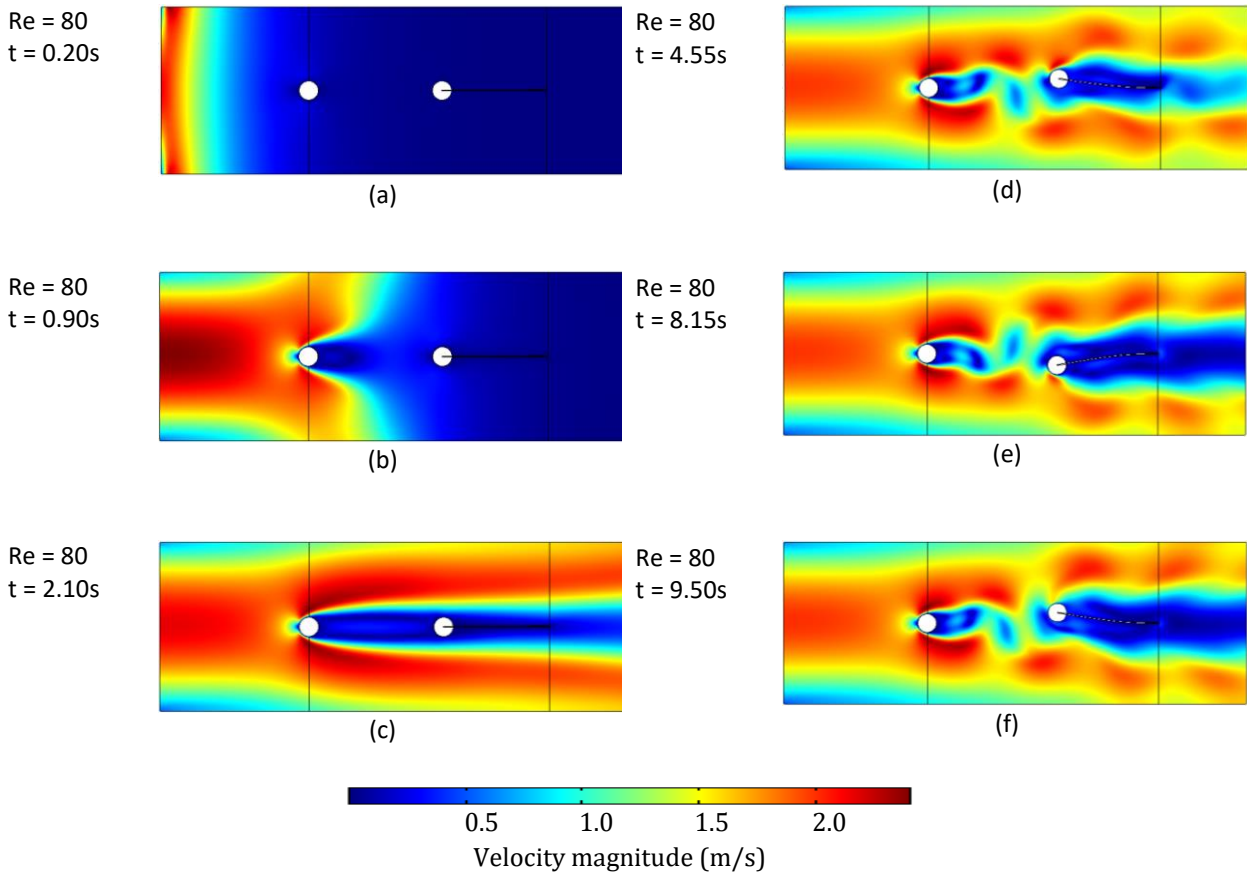

Fig. 5. Velocity magnitude flow patterns for 2D simulation at Re 80 (a) Simulation time taken at t = 0.20s (b) Simulation time taken at t = 0.90s (c) Simulation time taken at t = 2.10s (d) Simulation time taken at t = 4.55s (e) Simulation time taken at t = 8.15s (f) Simulation time taken at t = 9.50s

The next approach is to obtain the lift force generated by every Reynolds number and gap length in the time domain. The pressure distribution around the bluff body needs to be calculated to analyze the external force around the bluff body. The lift force represents the aerodynamic force exerted on a bluff body when it interacts with fluid flow. This force acts perpendicular to the direction of the flow and is responsible for inducing oscillatory motion in the body. The lift force can be expressed as follows:

$$F_{lift} = \text{intop1}\ (\text{spf.T\_stressy}) \tag{3}$$

Where intop1 is an introduced integral operator and *spf.T_stressy* is the total stress on the surface of the bluff body along the y-axis direction.

Figure 6(a) shows the example data for the lift force at Re 80. In this research, the lift force is converted into a lift coefficient, as it serves as a versatile and standardized metric for assessing and contrasting the aerodynamic lift capabilities across diverse experiment setups. The equation of lift coefficient is shown in Eq. (4)

$$C_L = F_L/(\tfrac{1}{2}\rho_w U^2 D) \tag{4}$$

Where F_L is the lift force, ρ_W is a constant parameter for water density, U is the velocity of the object relative to the water, and D is the characteristic diameter.

The fluctuating lift force displaces the downstream cylinder shown in Figure 6(b), causing vibrations in the cantilever beam. These cantilever beam vibrations facilitate the transformation of mechanical energy into electrical energy through a piezoelectric sheet. Figure 6(c) shows the voltage generated by the piezoelectric at Re 80.

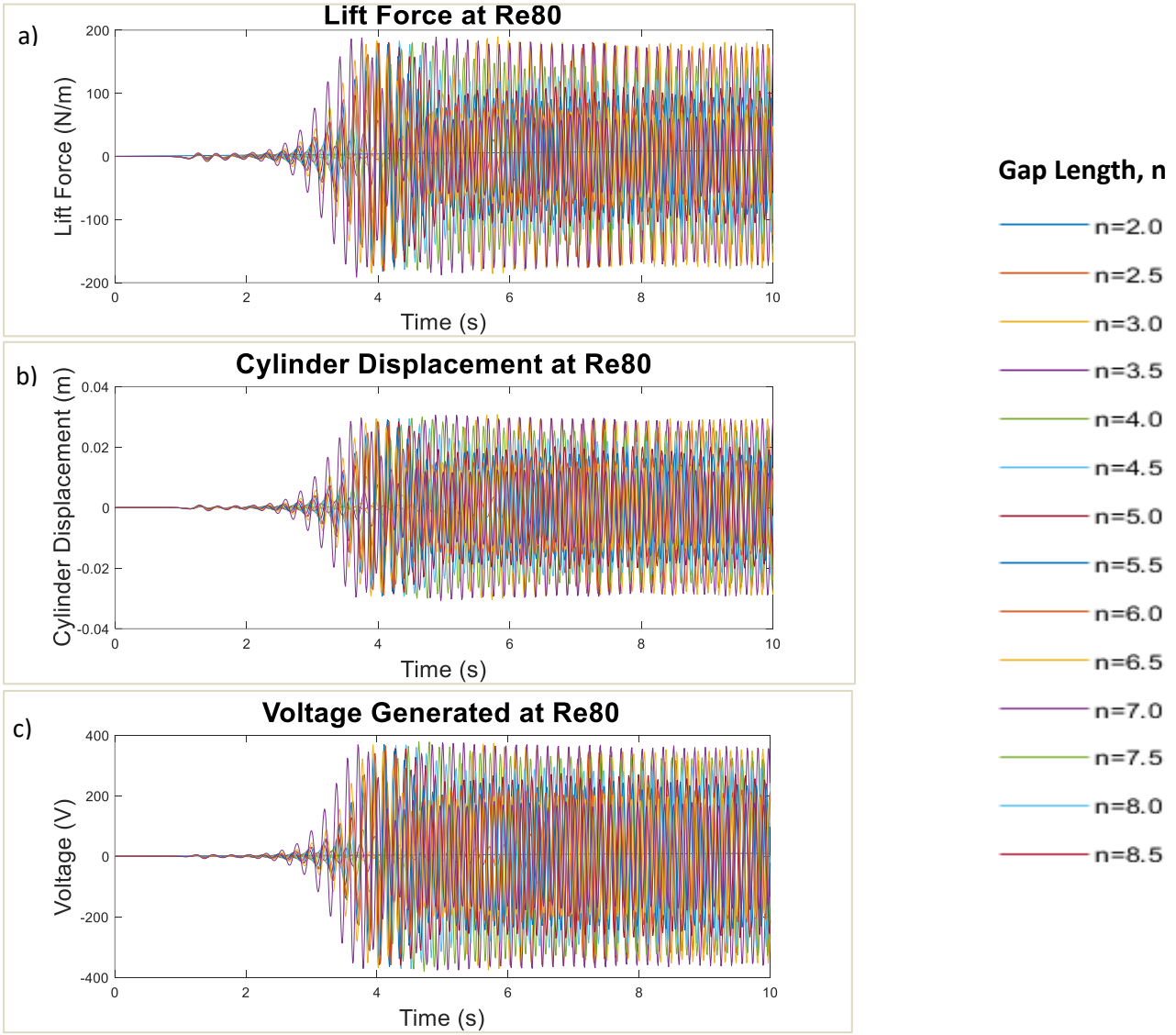

Fig. 6. Graph of simulation at Re 80 (a) Lift force (b) Cylinder displacement (c) Voltage generated

The last step of data collection is determining the power generated by each Reynolds number. Fast Fourier Transform (FFT) is used to transform a time-domain signal into a frequency-domain representation. Converting a time-domain signal into a frequency-domain signal allows for the determination of the system's frequency, which can be compared to the natural frequency of the beam to produce resonance, resulting in the highest voltage in the system. It also helps in the process of extracting the data from the graph, which allows for a clearer understanding during the analysis process. The data on voltage and current are collected to determine the power generated. The dot product is used instead of normal multiplication, as normal multiplication will reduce the system frequency by half. Therefore, the voltage generated in the frequency domain will be multiplied using

the dot product with the current generated in the frequency domain to obtain power in the frequency domain.

4. Simulation Data and Analysis

This section comprises three main components. The first component involves the analysis of data on lift coefficient, cylinder amplitude, voltage generated, and power generated using contour graphs. The next section will observe power generation at different Reynolds numbers in the frequency domain. Finally, the last part examines the optimal gap length required for maximizing power output at each Reynolds number.

4.1 Power Generation in Frequency Domain

The simulation resulted in a maximum lift coefficient of 4.22 at Re 80 and a gap length of 6.0, as illustrated in Figure 7(a). The lift coefficient value is nearly zero at gap lengths of 2.0–4.0, indicating the absence of wake production at the downstream cylinder. After a gap length of 6.0, the lift coefficient's value begins to decline. Five more peaks, at Re 60, 100, 120, 140, and 160, represent the highest lift coefficients in every Reynolds number, with respective values of 0.96, 1.53, 0.96, 1.08, and 1.35.

The cylinder amplitude graph in Figure 7(b) shows a similar pattern. The simulation created a most significant amplitude of 0.0144 m at Re 80 and a gap length of 6.0, which is 34.5% more than the second-highest peak at Re 100 and a gap length of 3.0. The data collected during Re 60 stayed low, never exceeding 0.0025 m. The lift force and cylinder amplitude are directly proportional; as the lift force increases, so will the cylinder amplitude.

As shown in Figure 7(c) and Figure 7(d), the highest voltage and power outputs were observed at a gap length of 6.0 with a Reynolds number of 80. However, beyond this peak, both the voltage and power values begin to decline. Nevertheless, even with this decrease, the voltage and power output remain significant for energy harvesting purposes. This graph provides valuable information within the range of gap lengths from 5.0 to 8.5. Additionally, at Re 100, significant values are observed from gap length 3.0 to 5.0 before a drastic decline occurs. The simulation at gap length 3.0 yields the second-highest voltage and power output throughout the experiment. For Re 120, the vortex behind the bluff body is formed at gap length 3.0, while for Re 140, the wake forms at gap length 3.5. The wake formation at Re 160 commences later at gap length 4.0. The highest peak for this Reynolds number is at gap length 4.5 before the output begins to decline.

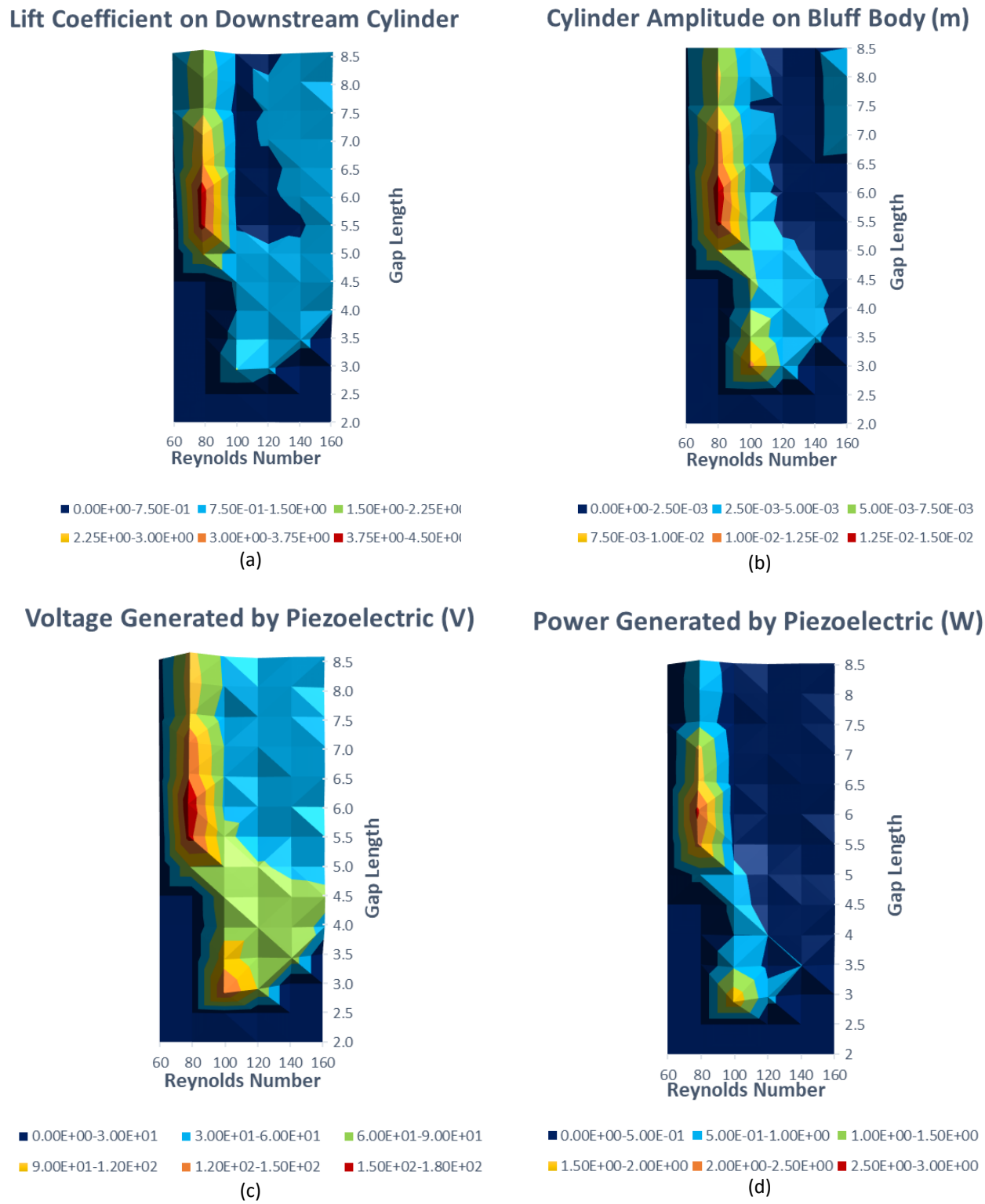

Fig. 7. 3D surface graph analysis: Examining the relationship between gap length, Reynolds number and power generated

In the field of fluid dynamics, a validation study has been conducted to assess the lift coefficient within a laminar flow environment characterized by a Reynolds number of 100. This study compares the simulation results with findings from four earlier investigations conducted by Braza *et al.,* [20], Calhoun [21], Liu *et al.,* [22], and Hassim *et al.,* [19]. The outcomes of this comparative analysis are presented concisely in Table 2.

Table 2
The lift coefficient in relation to previous studies (± is the amplitude oscillation)

Re = 100	
Published data	**Lift coefficient (C_L)**
Braza *et al.,* [20]	±0.250
Calhoun [21]	±0.298
Liu *et al.,* [22]	±0.339
Hassim *et al.,* [19]	±0.275
Present	±0.503

The study's primary goal is to achieve the most consistent output at each Reynolds number. The collected data on power generated from six sets of experiments has been compiled in Figure 8. The most consistent output value is mentioned at the peak of the highest data.

In Figure 8(a), the highest power generated at Re 60 is observed at a frequency of 0.8984 Hz, which results in a power generation of 0.03151 W. As the study progresses to Re 80, it shows a significant increase in the highest power output compared to the previous data, generating 2.617 W at a frequency of 1.25 Hz. The power generated increased by 275% compared to the average highest output for every Reynolds number. However, the power generation exhibits a decreasing trend at Re 100, which drops to 1.899 W at a frequency of 1.445 Hz, as illustrated in Figure 8(c). The highest power generated at Re 120 and 140 continues to decline to 0.655 W and 0.5 W, respectively. At the same time, the frequency of the system increases. Lastly, the graph Re 160 shows the increasing trend for frequency and power generated at 3.164 Hz and 0.3782 W, respectively. The frequency of the highest power generated at each Reynolds number has an increasing pattern as the Reynolds number increases.

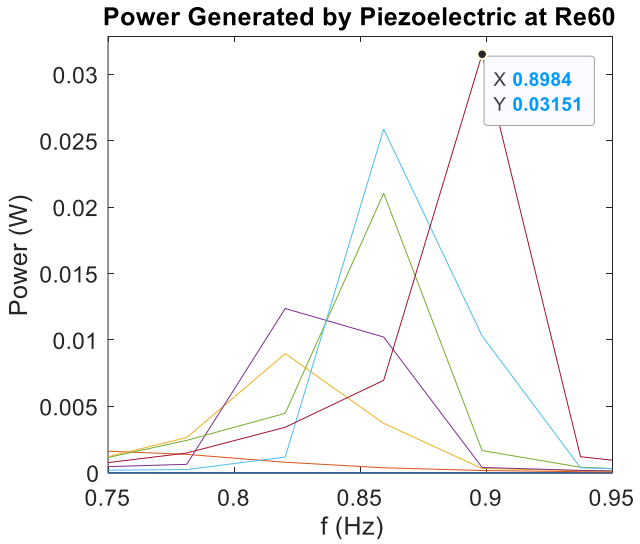

(a)

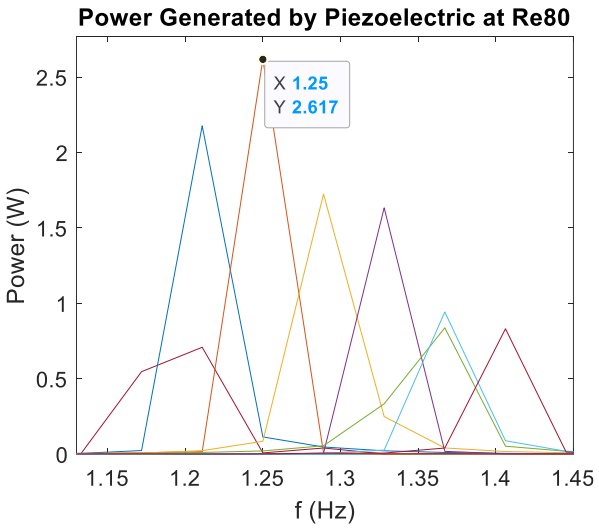

(b)

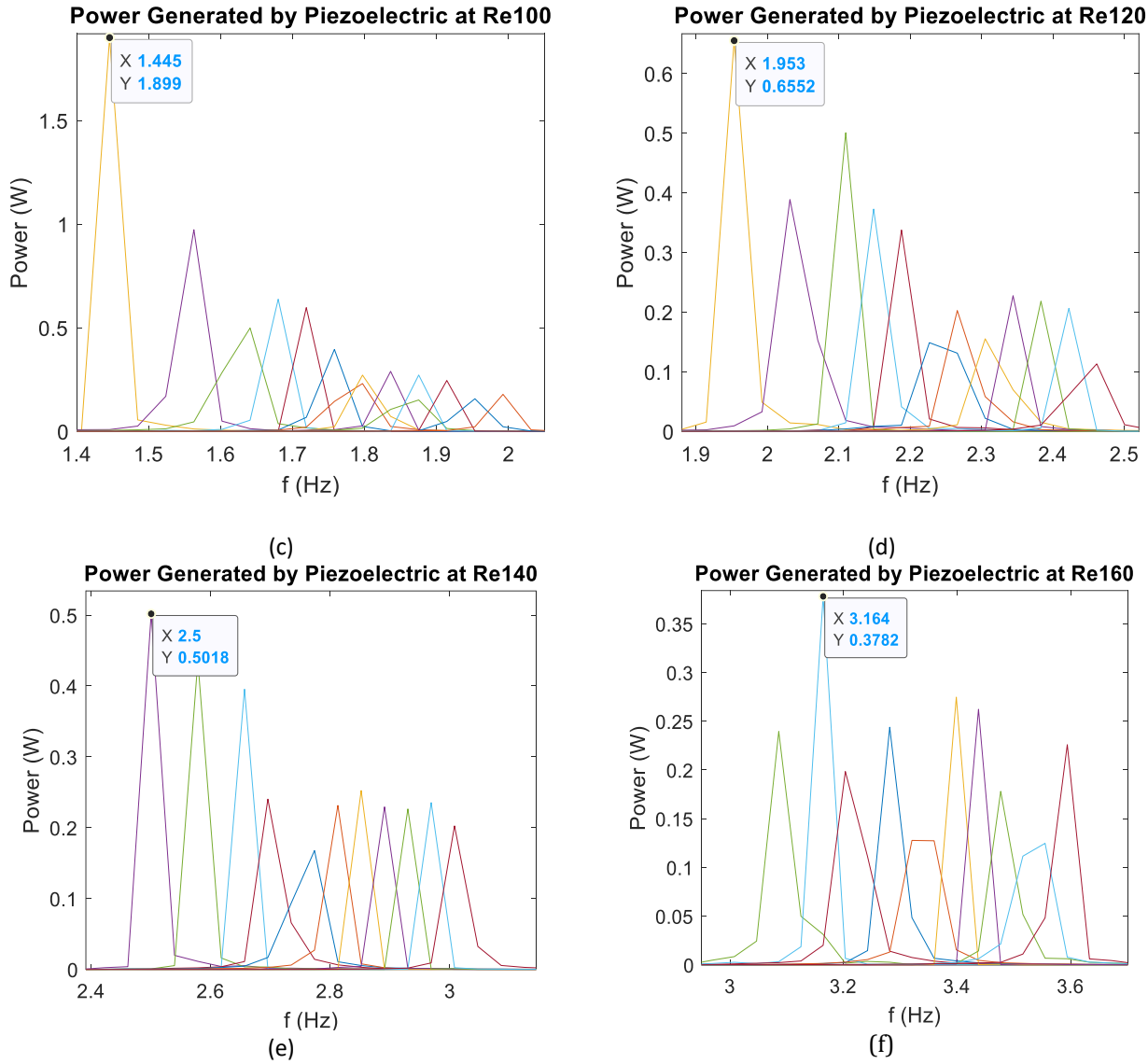

Fig. 8. Graph of power generated in frequency domain at difference number of gap length (a) The output power (Re = 60) (b) The output power (Re = 80) (c) The output power (Re = 100) (d) The output power (Re = 120) (e) The output power (Re = 140) (f) The output power (Re = 160)

4.2 Optimal Gap Length for Maximum Power Output

The graph of the Reynolds number versus the maximum power produced is shown in Figure 9. Reynolds number 60 yields the lowest power output among all the Reynolds numbers, with a maximum power generated of only 0.0315 W. The vortex creation during the simulation of Re 60 takes longer to build up compared to other Reynolds numbers. Therefore, the time to generate power is shorter than in other simulations. In contrast, simulations at Re 80 exhibit the highest power output consistently. The optimal gap length for Re 80 is at 6.0, yielding 2.617 W of power. Power generation at this Reynolds number steadily increases from gap length 5.0 to 6.0, reaching its peak. However, it begins to decline from gap length 6.5 to 7.0, followed by a drastic drop beyond gap length 7.5 until the end of the parameter range at 8.5. At Re 100, the second peak in power output is observed at gap length 3.0, generating 1.899 W of power. Other gap lengths at this Reynolds number yield power outputs below 1 W. For Re 120, the peak power output is 0.6552 W at a gap length of 3.0, with other gap lengths yielding power outputs ranging between 0.1 and 0.5 W. Similarly, the

optimal gap lengths for Re 140 and Re 160 are at 3.5 and 4.5, respectively, generating 0.5018 W and 0.3782 W of power.

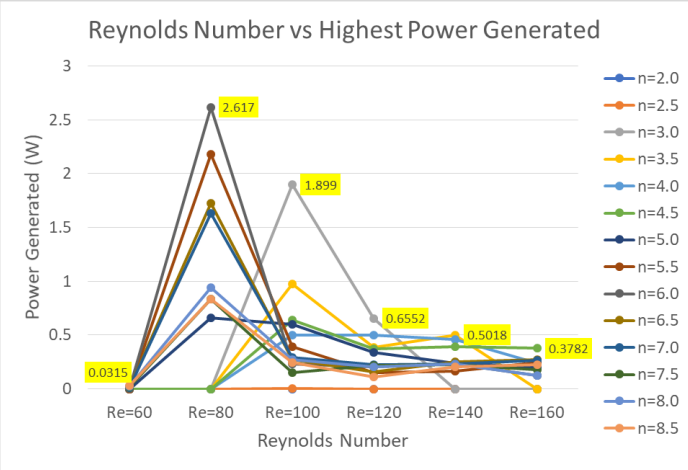

Fig. 9. Reynolds number vs. highest power generated graph

5. Conclusion

In conclusion, this study primarily examines the interaction of laminar flow with two circular cylinders arranged in tandem within an open-channel flow. The results highlight the optimal gap length between the cylinders for each Reynolds number. Notably, at Reynolds number 80, a gap length of 6.0 generates the maximum power output throughout the simulation. Higher lift forces around the downstream cylinder increase the amplitude and frequency of the cylinder oscillation. Hence, increase power generation. The other optimal gap lengths for Re 60, 100, 120, 140, and 160 are at 8.5, 3.0, 3.0, 3.5, and 4.5, respectively, and generate power outputs of 0.0315 W, 1.899 W, 0.6552 W, 0.5018 W, and 0.3782 W. This investigation establishes the correlation between Reynolds number and gap length, offering valuable insights into optimising flow-induced vibration (FIV) energy harvesting.

Acknowledgement

This research was funded by a grant from IIUM-UMP-UiTM Sustainable Research Collaboration Grant 2020 (SRCG20-034-0034).

References

[1] Japar, Wan Mohd Arif Aziz, Nor Azwadi Che Sidik, Natrah Kamaruzaman, Yutaka Asako, and Nura Mu'az Muhammad. "Hydrothermal performance in the Hydrodynamic Entrance Region of Rectangular Microchannel Heat Sink." *Journal of Advanced Research in Numerical Heat Transfer* 1, no. 1 (2020): 22-31.

[2] Xu, Zidong, Hao Wang, Chenxi Xing, Tianyou Tao, Jianxiao Mao, and Yun Liu. "Physics guided wavelet convolutional neural network for wind-induced vibration modeling with application to structural dynamic reliability analysis." *Engineering Structures* 297 (2023): 117027. https://doi.org/10.1016/j.engstruct.2023.117027

[3] Zhang, Lei, Lin Cheng, Hengyang Li, Jiaying Gao, Cheng Yu, Reno Domel, Yang Yang, Shaoqiang Tang, and Wing Kam Liu. "Hierarchical deep-learning neural networks: finite elements and beyond." *Computational Mechanics* 67 (2021): 207-230. https://doi.org/10.1007/s00466-020-01928-9

[4] Pinar, Engin, Tahir Durhasan, Göktürk M. Ozkan, Muhammed M. Aksoy, Huseyin Akilli, and Besir Sahin. "The effects of perforated cylinders on the vortex shedding on the suppression of a circular cylinder." In *EPJ Web of Conferences*, vol. 143, p. 02094. EDP Sciences, 2017. https://doi.org/10.1051/epjconf/201714302094

[5] Zahari, M. A., and S. S. Dol. "Effects of different sizes of cylinder diameter on vortex-induced vibration for energy generation." *Journal of Applied Sciences* 15, no. 5 (2015): 783-791. https://doi.org/10.3923/jas.2015.783.791

[6] Atrah, Ahmed B., Mohd Syuhaimi Ab-Rahman, Hanim Salleh, Mohd Zaki Nuawi, Mohd Jailani Mohd Nor, and Nordin Bin Jamaludin. "Karman vortex creation using cylinder for flutter energy harvester device." *Micromachines* 8, no. 7 (2017): 227. https://doi.org/10.3390/mi8070227

[7] Naseer, Rashid, Huliang Dai, Abdessattar Abdelkefi, and Lin Wang. "Comparative study of piezoelectric vortex-induced vibration-based energy harvesters with multi-stability characteristics." *Energies* 13, no. 1 (2019): 71. https://doi.org/10.3390/en13010071 [8] Zhang, Min, and Junlei Wang. "Experimental Study on Piezoelectric Energy Harvesting from Vortex-Induced Vibrations and Wake-Induced Vibrations." *Journal of Sensors* 2016, no. 1 (2016): 2673292. https://doi.org/10.1155/2016/2673292

[9] Han, Peng, Qiaogao Huang, Guang Pan, Wei Wang, Tianqi Zhang, and Denghui Qin. "Energy harvesting from flow-induced vibration of a low-mass square cylinder with different incidence angles." *Aip Advances* 11, no. 2 (2021). https://doi.org/10.1063/5.0037071

[10] Abdelkefi, A., M. R. Hajj, and A. H. Nayfeh. "Piezoelectric energy harvesting from transverse galloping of bluff bodies." *Smart Materials and Structures* 22, no. 1 (2012): 015014. https://doi.org/10.1088/0964-1726/22/1/015014

[11] Shao, Ze, Tongming Zhou, Hongjun Zhu, Zhipeng Zang, and Wenhua Zhao. "Amplitude enhancement of flow-induced vibration for energy harnessing." In *E3S Web of Conferences*, vol. 160, p. 01005. EDP Sciences, 2020. https://doi.org/10.1051/e3sconf/202016001005

[12] Assi, Gustavo RS. "Wake-induced vibration of tandem cylinders of different diameters." *Journal of Fluids and Structures* 50 (2014): 329-339. https://doi.org/10.1016/j.jfluidstructs.2014.07.001

[13] A´ ssi, Gustavo RS, Julio R. Meneghini, José AP Aranha, Peter W. Bearman, Bruno S. Carmo, and Enrique Casaprima. "Experimental investigation of flow-induced vibrations interference between two circular cylinders in tandem arrangements." In *International Conference on Offshore Mechanics and Arctic Engineering*, vol. 41952, pp. 273-277. 2005.

[14] Fan, Xiantao, Zhongchen Wang, Xiaoyu Chen, Yang Wang, and Wei Tan. "Experimental investigation on flow-induced vibration of flexible multi cylinders in atmospheric boundary layer." *International Journal of Mechanical Sciences* 183 (2020): 105815. https://doi.org/10.1016/j.ijmecsci.2020.105815

[15] Dahl, J. M., F. S. Hover, M. S. Triantafyllou, and O. H. Oakley. "Dual resonance in vortex-induced vibrations at subcritical and supercritical Reynolds numbers." *Journal of Fluid Mechanics* 643 (2010): 395-424. https://doi.org/10.1017/S0022112009992060

[16] Wang, Huakun, Dongliang Zhao, Wenyu Yang, and Guoliang Yu. "Numerical investigation on flow-induced vibration of a triangular cylinder at a low Reynolds number." *Fluid Dynamics Research* 47, no. 1 (2014): 015501. https://doi.org/10.1088/0169-5983/47/1/015501

[17] Raghavan, K., and M. M. Bernitsas. "Experimental investigation of Reynolds number effect on vortex induced vibration of rigid circular cylinder on elastic supports." *Ocean Engineering* 38, no. 5-6 (2011): 719-731. https://doi.org/10.1016/j.oceaneng.2010.09.003

[18] Govardhan, R. N., and C. H. K. Williamson. "Defining the 'modified Griffin plot' in vortex-induced vibration: revealing the effect of Reynolds number using controlled damping." *Journal of fluid mechanics* 561 (2006): 147-180. https://doi.org/10.1017/S0022112006000310

[19] Hassim, Muhammad Ridhwaan, Mohd Azan Mohammed Sapardi, Nur Marissa Kamarul Baharin, Syed Noh Syed Abu Bakar, Muhammad Abdullah, and Khairul Affendy Mohd Nor. "CFD Modelling of Wake-Induced Vibration At Low Reynolds Number." *CFD Letters* 13, no. 11 (2021): 53-64. https://doi.org/10.37934/cfdl.13.11.5364

[20] Braza, M., P. H. H. M. Chassaing, and H. Ha Minh. "Numerical study and physical analysis of the pressure and velocity fields in the near wake of a circular cylinder." *Journal of fluid mechanics* 165 (1986): 79-130. https://doi.org/10.1017/S0022112086003014

[21] Calhoun, Donna. "A Cartesian grid method for solving the two-dimensional streamfunction-vorticity equations in irregular regions." *Journal of computational physics* 176, no. 2 (2002): 231-275. https://doi.org/10.1006/jcph.2001.6970

[22] Liu, C., X. Zheng, and C. H. Sung. "Preconditioned multigrid methods for unsteady incompressible flows." *Journal of Computational physics* 139, no. 1 (1998): 35-57. https://doi.org/10.1006/jcph.1997.5859